Embedded-cluster calculations for transition-metal impurities in $BaTiO_3$

1996 J. Phys.: Condens. Matter 8 1687

(http://iopscience.iop.org/0953-8984/8/11/013)

J. Phys.: Condens. Matter **8** (1996) 1687–1704. Printed in the UK

Embedded-cluster calculations for transition-metal impurities in $BaTiO_3$

H Donnerberg†§ and R H Bartram‡

† University of Osnabrück, FB Physik, D-49069 Osnabrück, Germany
‡ University of Connecticut, Department of Physics, Storrs, CT 06269-3046, USA

Received 26 October 1995

Abstract. The embedded-cluster technique is used to simulate the local electronic structure of transition-metal impurities in $BaTiO_3$. The description of the central defect cluster employs an *ab initio* SCF-MO approach. The quantum cluster consists of 21 ions. Outer crystal regions are modelled on the basis of a shell-model representation. In all cases defect-induced lattice relaxations have been consistently included. Our results, demonstrated for Mn_{Ti}^{4+}, concern optical transitions, Jahn–Teller effects and questions related to the stability of this defect. The computational level of our *ab initio* calculations corresponds to Hartree–Fock theory (HF) and the configuration interaction (CI). Additionally, Møller–Plesset perturbation theory and density functional theory have been applied to investigate charge-transfer transitions.

1. Introduction

$BaTiO_3$ represents an important photorefractive material with interesting prospects for technological applications. It is well documented that transition-metal cations doped into this perovskite play a central role for photorefractivity to occur [1, 2]. Also, the development of tunable solid-state lasers is based on transition-metal impurities in suitable host systems [3].

Theoretical investigations of point defect centres, of which transition-metal impurities form a subset, aim to address all of the important questions related to the electronic and structural properties of defects. For this purpose, basically three approaches are known to be adequate: full electron supercell simulations which are in the spirit of perfect-crystal bandstructure calculations, Green's function treatments and embedded-quantum-cluster calculations. We employ the latter approach, since only this one easily allows us to study the local electronic defect structure of charged point defects taking full account of lattice relaxations. This is accomplished by representing the embedding lattice on the basis of a pair-potential shell-model description. Defect-induced lattice distortions are to be expected in $BaTiO_3$ because of the semi-ionic bonding properties of this oxide material. Green's function approaches and supercell calculations, on the other hand, are much more restricted to neutral defects and are less well suited to including lattice distortions. Their success is mainly related to a description of defects in semiconductors.

So far, embedded-cluster simulations have been reported for a number of different defect species in ionic materials including impurity cations, anion vacancies and hole-type defects in alkali halides, elpasolites and in basic binary oxides such as MgO (see, for example, [4–8]). In the present contribution we discuss the details of our previous investigations [9]

§ E-mail address: hdonner@physik.uni-osnabrueck.de.

0953-8984/96/111687+18$19.50

on $BaTiO_3$:Mn^{4+}_{Ti}. The reason for choosing Mn^{4+} as a test case of our simulations is based on the observation that this impurity cation represents a neutral defect when substituting for Ti^{4+}. Further, Mn^{4+} is isoelectronic to the important Cr^{3+}. We have chosen $BaTiO_3$ as the host material because of its technological importance. Unfortunately, there is no experimental information for Mn^{4+} in cubic $BaTiO_3$. It has been argued [10, 11] that the pronounced dynamical order–disorder effects leading to ferroelectricity affect the Mn^{4+} and are responsible for the absence of data. In order to compensate for this deficiency we compare our calculations with observations for the isoelectronic $SrTiO_3$:Mn^{4+}, instead. The two perovskite oxides are structurally very similar; however, unlike the barium compound, $SrTiO_3$ remains paraelectric at all temperatures.

Our results, which concern optical crystal-field (CF) transitions, defect-induced lattice relaxations, Jahn–Teller distortions related to the excited $^4T_{2g}$ state and charge-transfer (CT) transitions, have been obtained by applying a Hartree–Fock (HF) treatment to a central 21-atom quantum cluster. Most of these calculations are further compared with more advanced simulations employing an extensive configuration interaction description in order to include important electron correlation contributions. Moreover, auxiliary calculations based on Møller–Plesset perturbation theory and density functional theory have been performed to indicate the importance of correlations with respect to charge-transfer transitions.

By including electron correlations and charge-transfer transitions the present work extends the methods of previous investigations [6].

2. Method

A quantum chemical description of a central defect cluster is at the heart of any embedded-cluster calculation (ECC). The various existing ECC can be distinguished with respect to the size of the cluster and to the representation of the embedding lattice. Other differences address the level of sophistication of the quantum mechanical calculations. Possible choices relate to the use of Hartree–Fock or density functional theory (DFT), of which the latter approach is known to be particularly well suited for electronic ground states. Since our investigations aim at the accurate characterization of both ground and excited states, we decided to mainly employ the HF one-electron approximation (if not explicitly stated we used the restricted open-shell HF approximation) augmented with suitable correlation treatments. Auxiliary DFT calculations, on the other hand, have been restricted to investigations of charge-transfer transitions. Employing ground-state functional Kohn–Sham theory, the calculated energy separations between ground and excited states provide in most cases lower bounds to the exact energy differences. However, the quality of such lower bounds must in any instance be judged on the basis of different exact calculations. For a brief discussion and corresponding results, refer to section 3.3.

The large number of two-electron exchange integrals, which need to be calculated and stored prior to the SCF procedure implementation, forced us to include only a limited number of atoms in our quantum calculation. Further constraints on the cluster size were implied by our configuration interaction expansion. Therefore, following a reasonable compromise we employed *ab initio* LCAO-MO calculations for a central $MO_6Ba_8Ti_6$ defect cluster, which simulates the crystal lattice immediately neighbouring an M_{Ti} transition-metal impurity cation in $BaTiO_3$. The perfect-crystal structure has been assumed according to the cubic high-temperature phase. The resulting 21-atom defect cluster $MO_6Ba_8Ti_6$ is shown in figure 1.

All subsequently reported results refer to tetravalent manganese Mn^{4+}. To model the electronic structure of the cluster, effective-core potentials (ECP) were employed in

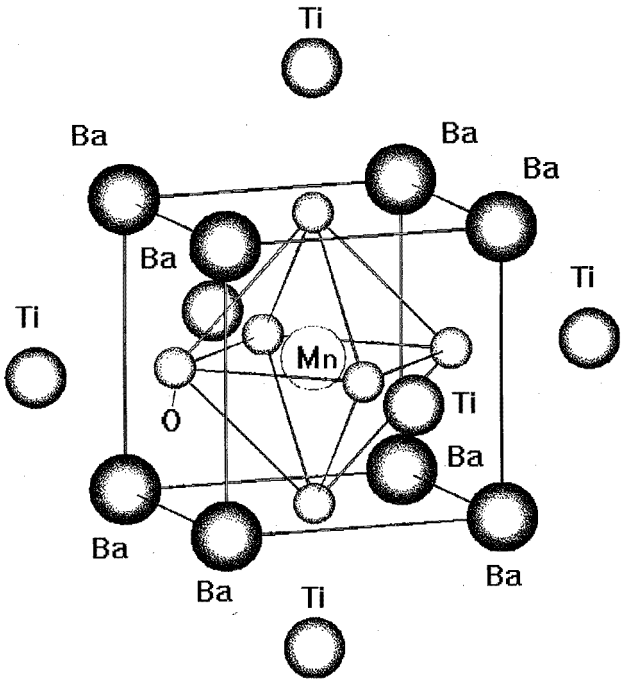

Figure 1. The quantum mechanical defect cluster. The immediate environment of the central MnO_6 complex consists of eight barium and six titanium cations which are represented by bare effective-core potentials.

conjunction with double-zeta-quality basis functions for the valence orbitals on manganese [12] and Dunning's contractions of Huzinaga's basis set for the oxygen ions [13]. The oxygen basis set was further augmented with diffuse p and polarizing d functions. The outer Ba and Ti ions were represented by bare effective-core potentials which simulate ion-size effects of these cations. The *ab initio* ECP parametrization has been taken from Hay and Wadt [12].

The formal cation charges used in this publication should not be understood to indicate any pronounced ionicities of the systems considered. Instead, the notation is intended to characterize the electronic open-shell structure of the (impurity) cations investigated; e.g. Mn^{4+} denotes a $3d^3$-type open-shell configuration of manganese. Our calculations confirm that there are generally significant hybridizations within the central MO_6 octahedron (particularly between the O 2p and the nd orbitals of the transition-metal cation M). Nevertheless, Mn^{4+} represents a neutral lattice defect in the sense that the corresponding MnO_6 complex carries the same total charge as the substituted intrinsic TiO_6 complex (i.e. $-8|e|$).

Besides HF theory we mainly used configuration interaction (CI) expansions to represent important electronic correlation contributions. These calculations were restricted to the inclusion of single and double electronic excitations (SDCI) with reference to the respective HF states. On the basis of perturbation theory the 15 000 energetically most important configurations were chosen for a further diagonalization of the CI Hamiltonian matrix (the perturbation energy contribution of these retained states is denoted by PEK, and the contribution of all neglected states by PEN). This procedure follows the earlier approach of

Table 1. Calculated crystal-field splittings employing the various types of CI as introduced in the text. The cluster geometry corresponds to cubic perfect-lattice spacings.

Type of CI	$\Delta_{CF} = E(^4T_{2g}) - E(^4A_{2g})$ (eV)
SDCI	1.15
SDCI + Q	2.48
NO-SDCI	2.11
NO-SDCI + Q	2.23

Rawlings and Davidson [14]. Size consistency has been approximated using the formula of Davidson and Silver [15]:

$$E_{corr}(\text{SDCI} + Q) = E_{HF} + \frac{c_{HF}^2}{2c_{HF}^2 - 1}\left[1 - \frac{\text{PEN}}{\text{PEK}}\right](E_{corr}(\text{SDCI}) - E_{HF}) \tag{1}$$

where c_{HF} is the expansion coefficient of the HF wavefunction and E_{corr}(SDCI) the uncorrected SDCI energy. The stability of these SDCI($+Q$) results has been further tested by calculating the natural orbitals, which by construction diagonalize the (SDCI) first-order reduced density matrix, and iterating the configuration interaction with these orbitals (the NO-SDCI($+Q$) procedure [16]). It is recalled that natural orbitals provide the most rapidly convergent CI expansion. In this sense the NO-SDCI($+Q$) results are superior to those of the SDCI($+Q$) employing HF orbitals. Table 1 compiles energy separations between electronic crystal-field states of Mn^{4+} which have been calculated employing these various CI approaches. In all cases we found that the SDCI + Q results are superior to those for the uncorrected SDCI. The best results correspond to the NO-SDCI + Q level. As these calculations involve unreasonably large computer capacities, we employed the following compromise: the SDCI + Q method has been used to determine the required total energy surfaces of the cluster, which were needed to perform the embedded-cluster relaxation step (see below). Finally, energy separations have been recalculated for the relaxed equilibrium configurations on the basis of the NO-SDCI + Q method. Therefore, if not explicitly specified, all subsequently reported CI energy differences correspond to the NO-SDCI + Q level. The cluster *ab initio* calculations have been performed using the quantum chemical program packages MELDF [17] and HONDO 7.0 [18]. The CADPAC code [19] has been employed to perform additional charge-transfer calculations based on Møller–Plesset perturbation theory and DFT (see section 3.3).

In the present work the embedding lattice was simulated by means of an interionic effective-pair-potential model, i.e. the shell model [20]. By construction, crystal ions consist of a massive core (charge X) to which the shell of valence electrons (charge Y) is harmonically bound (with spring constant k); the sum $Q = X + Y$ specifies the total integral ion charges. The free-electronic polarizability of the crystal ions is given by

$$\alpha = \frac{Y^2}{k}. \tag{2}$$

Further pair potentials act between the components of different ions. Besides long-range Coulomb potentials, short-range interactions must be included, which represent the interionic repulsion, correlation and covalency contributions. The functional form of these short-range potentials has been taken as a Buckingham potential:

$$V(r) = A\ \exp(-r/\rho) - \frac{C}{r^6}. \tag{3}$$

It is noted that short-range potentials arising from electronic interactions are defined between different ion shells.

The minimization of the lattice energy as a function of core and shell coordinates yields the equilibrium configuration of perfect and defective lattices. In order to simulate isolated defects a two-region strategy is employed by means of which the crystal is partitioned into two regions: the inner region immediately surrounding the specified defect usually contains ~300 ions and is treated atomistically, which means that this region is fully relaxed to its equilibrium structure according to the underlying potentials; the outer region, i.e. the remaining crystal, is described on the basis of the continuum theoretical Mott–Littleton approximation [21]. The method is coded in the computer program CASCADE [22] which is used in the present investigations. For details of solid-state computer simulations we refer the reader to the monograph edited by Catlow and Mackrodt [23]. All potential parameters appropriate for $BaTiO_3$ and for impurity–oxygen interactions have been taken from the extensive work of Lewis and Catlow [24]. These pair potentials have also been used to specify the interactions of the cluster ions with the embedding shell-model ions.

The total energy of the ECC-type crystal is minimized with respect to the cluster (nuclear) coordinates R_c and to core and shell coordinates R_o of the outer crystal ions. The additionally required minimization with respect to the cluster wavefunction Ψ describing the local electronic structure within the cluster region is performed by means of the *ab initio* HF(+CI)-SCF-MO calculations which were introduced above. The energy difference of the total energy of the quantum defect cluster $E_{QM}^{clus}(\Psi, R_c)$ corresponding to the electronic states Ψ of interest ($^4A_{2g}$ and $^4T_{2g}$ for Mn^{4+}) and its classical pair-potential counterpart $E_{SM}^{clus}(R_c)$ was calculated on a $5 \times 5 \times 5$ mesh of a_{1g}-symmetrical breathing-mode displacements δ of O^{2-}, Ba^{2+} and Ti^{4+} ions surrounding the central impurity cation. These energy values, fitted to a fourth-order polynomial

$$P_\Psi(\delta_O, \delta_{Ba}, \delta_{Ti}) = E_{QM}^{clus}(\Psi, R_c) - E_{SM}^{clus}(R_c) = \sum_{n+m+p\leqslant 4} A_{nmp}\delta_O^n\delta_{Ba}^m\delta_{Ti}^p \qquad (4)$$

in the three types of displacement, were used to update the total pair-potential crystal energy and gradients so as to include the embedding shell model as well as the quantum cluster contributions. The total energy of the ECC crystal is given by

$$E(\Psi, R_c, R_o) = E_{SM}^{crys}(R_c, R_o) + P_\Psi(\delta_O, \delta_{Ba}, \delta_{Ti}) \qquad (5)$$

with

$$R_c(i) = R_c^0(i) + \delta_i \qquad (i = O, Ba, Ti). \qquad (6)$$

R_c^0 denotes the unrelaxed positions of cluster ions; $E_{SM}^{crys}(R_c, R_o)$ is the shell-model energy of the total crystal. The total crystal energy obtained from equation (5) comprises the substitution for a pair-potential defect cluster of its quantum mechanical counterpart. The short-range cluster–lattice interaction is modelled on the basis of the known pair potentials. A rigorous basis for equation (5) can be given by the group function theory of McWeeny [25] and Huzinaga and Cantu [26]. Further approximations then refer to the representation of the cluster environment on the basis of a shell-model description.

The final crystal relaxation was performed using a modified version of the shell-model program CASCADE [27]. Modifications of CASCADE were found to be necessary, because the quantum cluster energy models an exact image of the *ab initio* breathing-mode potential energy surface and, thus, goes beyond the pair-potential approximation as used in CASCADE. It is sufficient to update only the energy and gradients appropriately, since CASCADE employs the variable-metric technique to minimize the crystal energy. Thus,

the inverse Hessian is iteratively approximated using the updated coordinates and gradients and, finally, converges to its exact form.

We emphasize in this context that we avoided constructing a tight link between the CASCADE code and the quantum chemical *ab initio* programs employed, in order to retain sufficient flexibility regarding the *ab initio* step of our simulations.

Table 2. Total ion relaxations within the first three neighbour shells of Mn^{4+}_{Ti} ($^4A_{2g}$ and $^4T_{2g}$ state). −: inward relaxation; +: outward relaxation.

	$^4A_{2g}$-related ion relaxation (Å)		
Ion type	ECC(CI)	ECC(HF)	Shell model
O^{2-}	−0.035	−0.046	−0.240
Ba^{2+}	−0.347	−0.385	−0.190
Ti^{4+}	+ 0.113	+ 0.100	+ 0.01
	$^4T_{2g}$-related ion relaxation (Å)		
Ion type	ECC(CI)	ECC(HF)	Shell model
O^{2-}	−0.021	−0.037	−0.240
Ba^{2+}	−0.348	−0.370	−0.190
Ti^{4+}	+ 0.119	+ 0.106	+ 0.01

On the basis of the cubic symmetry employed in the present problem, the quantum mechanical cluster configuration can be determined from *in vacuo* cluster calculations. This is true, since the first non-vanishing terms of the electrostatic crystal potential are of fourth order and, further, the cluster multipole moments vanish up to the hexadecapole moment. Generalizations to systems exhibiting symmetry lower than cubic would in principle be straightforward; however, the computational costs increase rapidly with the additional degrees of freedom. Moreover, the total quantum energy of the cluster may no longer be determined independently of the embedding-lattice configuration.

3. Results

3.1. Lattice relaxations

Table 2 displays the calculated breathing-mode displacements of the three shells of ions which neighbour the central Mn impurity. The manganese was assumed to be in its electronic quartet states $^4A_{2g}$ and $^4T_{2g}$. Different degrees of approximation have been employed to account for the local electronic structure of the defect cluster, i.e. descriptions based on the shell model, and the HF and CI models. This order denotes the increasing flexibility of the electronic structure modelled. We emphasize that pure shell-model simulations are not able to reflect any changes which are related to the electronic state of the Mn ion (the corresponding columns in table 2 are thus replicas of each other).

Inspecting table 2 we observe that all results are in remarkable qualitative agreement: the pronounced inward relaxation of the Ba^{2+} ions, the outward relaxation of the Ti^{4+} ions and, finally, the inward relaxation of the oxygen ligands. The ligand relaxation is in agreement with ion size arguments, because $R(Mn^{4+}) < R(Ti^{4+})$ (see [28]). Its calculated size, however, depends on the degree of approximation applied to represent the electronic structure of the MnO_6 cluster. The more accurately it is described, the less are the calculated

ligand relaxations. Within the shell model the deficiencies of representing defect-induced electron redistributions are compensated by exaggerated displacements of the oxygen ions. In comparison the ECC-derived oxygen displacements are smaller by an order of magnitude. Table 2 further shows that the oxygen relaxations, particularly, are more pronounced, with the manganese cation being in its $^4A_{2g}$ ground state. Obviously, the excitation of the Mn^{4+} into the electronic $^4T_{2g}$ state slightly increases the manganese radius, since the excited state is more diffuse than the ground state. A similar argument may be applied to the CI which admixes extended excited states into the HF ground state which allows for Coulomb correlations.

Table 3. Total ion relaxations (Å) within the first three neighbour shells of a central Ti^{4+} cation. a: the bare ECP for the central Ti; b: the orbital representation analogous to Mn. −: inward relaxation; +: outward relaxation.

Ion type	a	b
O^{2-}	+0.073	−0.030
Ba^{2+}	+0.022	−0.130
Ti^{4+}	−0.029	+0.021

In order to distinguish between contributions due to a cluster–lattice mismatch and proper defect-induced relaxations we also calculated the ion displacements for a perfect cluster containing Ti^{4+} instead of Mn^{4+} as the central cation. These calculations (table 3) have been performed within the HF approximation. The CI is again expected to further reduce the oxygen ligand displacements. Two stages of a modelling are compared in table 3. The first refers to a representation of the central Ti cation using a bare effective-core potential (model a in table 3). This description is fully symmetric with respect to the outer Ti cations at the cluster boundary. There are no effects of covalency between cations and anions. In the second situation (model b) the electronic structure of the central Ti is treated equivalently to that of the Mn impurity; thus, only the 1s–2p core electrons are simulated by effective-core potentials, whereas the outer electronic structure is given explicitly. In this case the symmetry between the central and the outer Ti cations is broken, since covalency and charge transfer can take place between the oxygen anions and the central cation. Obviously, these effects most importantly affect the radial relaxation of the Ba cations. Allowing charge transfer onto the central Ti cation results in a pronounced inward displacement of the Ba ions. However, the overall compatibility between both cluster descriptions and the shell-model representation of the outer lattice is remarkable, since even the Ba displacements in model b correspond to only 3.25% of the lattice constant.

Finally, the differences between the manganese and the titanium cluster (model b) may be interpreted as purely impurity induced: $\delta_O = -0.016$ Å, $\delta_{Ba} = -0.255$ Å and $\delta_{Ti} = +0.079$ Å. These additional relaxations refer to the $^4A_{2g}$ ground state of Mn^{4+}. For the $^4T_{2g}$ state we obtain: $\delta_O = -0.007$ Å, $\delta_{Ba} = -0.240$ Å and $\delta_{Ti} = +0.085$ Å. The calculated defect-induced ligand relaxations (referring to $^4A_{2g}$) are in satisfactory agreement with reported effective-ion size differences (0.065 Å) [28]. Generally, the defect-induced relaxations will increase with increasing charge and size misfit of the impurity cation. Indeed, preliminary HF simulations for Cr_{Ti}^{3+} employing a smaller $3 \times 3 \times 3$ mesh of a_{1g}-type displacements yield the following defect-induced relaxations: $\delta_O = +0.068$ Å, $\delta_{Ba} = -0.27$ Å and $\delta_{Ti} = +0.12$ Å for the $^4A_{2g}$ state; and $\delta_O = +0.072$ Å, $\delta_{Ba} = -0.22$ Å and $\delta_{Ti} = +0.11$ Å for the $^4T_{2g}$ state. In particular, the outward displacements of the oxygen ions are larger by an order of magnitude than the reported radii differences between

Ti^{4+} and Cr^{3+} [28]. This result suggests the dominating effects to be due to charge misfit and confirms earlier shell-model-based simulations of Sangster [29].

Table 4. The energy separation between crystal-field states. oA: optical absorption; oE: optical emission.

	HF energy separation (eV) from $^4A_{2g}$ for different lattice geometries		
Electronic state	Undistorted	$^4A_{2g}$ relaxed	$^4T_{2g}$ relaxed
^2E_g	1.87	1.84	1.84
$^4T_{2g}$	2.31	2.56(oA)	2.53(oE)
	CI energy separation (eV) from $^4A_{2g}$ for different lattice geometries		
Electronic state	Undistorted	$^4A_{2g}$ relaxed	$^4T_{2g}$
^2E_g	1.65	1.65	—
$^4T_{2g}$	2.23	2.40(oA)	2.37(oE)

In the following sections we choose the total embedded-cluster relaxations (see table 2) over the purely defect-induced displacement contributions, because only the first represent fully *equilibrated* lattice structures.

3.2. Optical absorption and emission between crystal-field states

Table 4 displays the calculated energy separations between the excited $^4T_{2g}$ and ^2E_g states and the electronic ground state $^4A_{2g}$. In these calculations the ΔSCF method has been employed which takes into account all important orbital relaxation effects (see also section 3.3). Three different lattice geometries have been considered, i.e. observed perfect-lattice spacings and a_{1g} relaxed lattices corresponding to the $^4A_{2g}$ and $^4T_{2g}$ electronic states of Mn^{4+} (see section 3.1, table 2). The different lattice geometries obtained from HF and CI methods have also been taken into account. However, further JT distortions, which are to be expected for the orbitally degenerate excited states, were neglected at this stage. The transition energies calculated with respect to the $^4A_{2g}$ and $^4T_{2g}$ equilibrated lattices correspond to optical absorption and emission, respectively. We note that HF-derived excited-state energy separations from the ground state are 0.1–0.2 eV greater than the corresponding CI energy differences. Besides a direct energetical effect, which may be inferred by comparing HF and CI energy differences calculated in the *same* lattice structure (for example, compare the perfect-lattice results in table 4), there is an indirect effect which is based on the differences between the relaxation patterns produced by HF and CI (see section 3.1, table 2). In the case of the CI the smaller inward displacements of the oxygen ions lead to a reduction of the crystal-field splitting $E(^4T_{2g}) - E(^4A_{2g})$. For example, taking the two $^4A_{2g}$ equilibrated geometries of table 2 we obtain a reduction of 0.06 eV. Generally, the effect turns out to be $\leqslant$0.1 eV.

The calculated Stokes shift, i.e. the difference between absorption and emission energies, is small and equals 0.03 eV within HF and CI theory. The same order of magnitude has been found for Cr^{3+} doped into MgO [30]. Because there are no experimental data for Mn^{4+} in cubic $BaTiO_3$, we compare our results with those for $SrTiO_3$:Mn^{4+}: $E(^2E_g) - E(^4A_{2g}) = 1.71$ eV and $E(^4T_{2g}) - E(^4A_{2g}) = 2.14$–$2.23$ eV (absorption) [31, 32]. From the smaller lattice constant in this material there will be essentially no ligand relaxation

around an Mn^{4+} ion in $SrTiO_3$; thus the experimental energies for $SrTiO_3$:Mn^{4+} may safely be compared with calculated energies for $BaTiO_3$ which employ relaxed lattices. Whereas the ^2E_g-related separation is insensitive to lattice relaxations, there is a pronounced effect for $E(^4T_{2g}) - E(^4A_{2g})$. Our calculated absorption energies (CI) are greater by ∼0.2 eV than the reported experimental data. We believe that the relaxation contributions due to a cluster–lattice mismatch as discussed in section 3.1 are mainly responsible for this deviation. In spite of this feature the agreement between calculated and experimental energy separations is very encouraging. However, our results also suggest the importance of electron correlations in predicting accurate crystal-field splittings.

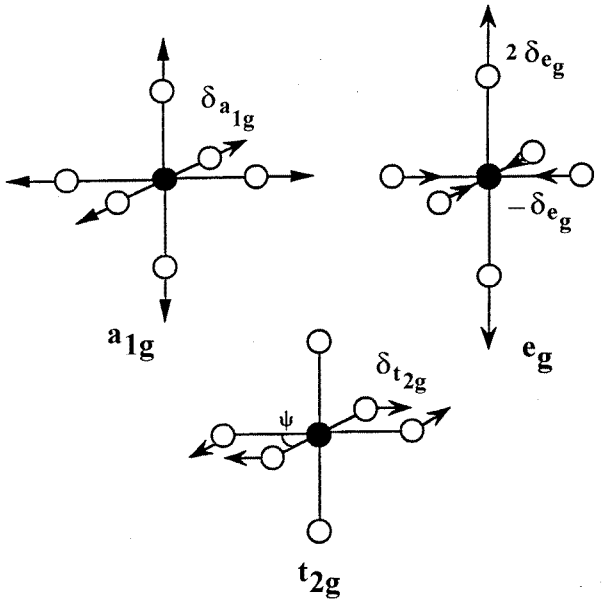

Figure 2. Symmetry-adapted a_{1g}, e_g and t_{2g} distortions of an MO_6 octahedron.

Table 5. The coupling of local e_g modes to $^4A_{2g}$ and $^4T_{2g}$. Note that $\delta(O_{\pm z}) = 2\delta_{e_g}$ and $\delta(O_{xy}) = -\delta_{e_g}$.

	HF		CI	
	$^4A_{2g}$	$^4T_{2g}$	$^4A_{2g}$	$^4T_{2g}$
δ_{e_g} (au)	—	−0.029	—	−0.017
E_{JT} (cm^{-1})	—	−290	—	−138
ω_{JT} (cm^{-1})	650	652	768	710

The orbital degeneracy of the excited $^4T_{2g}$ state leads under the action of appropriate electron–phonon couplings to the occurrence of symmetry-reducing Jahn–Teller distortions. These JT distortions were approximately treated by minimizing the total energy with respect to the symmetry-adapted displacements of the oxygen ligands with the remaining ions fixed in their a_{1g} relaxed positions corresponding to the $^4T_{2g}$ state. Figure 2 displays the symmetry-adapted normal modes of an octahedron. Principally, e_g $^4T_{2g}$ and t_{2g} $^4T_{2g}$

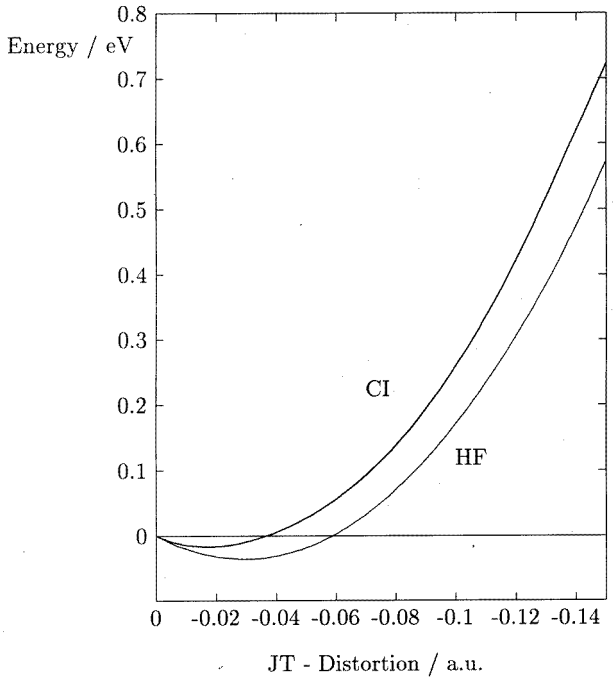

Figure 3. The e_g $^4T_{2g}$ Jahn–Teller effect. HF and CI potential energy curves are shown as a function of δ_{e_g}.

Table 6. Ion charges calculated from a MPA based on the excited Mn^{4+} $^4T_{2g}$ state. Further details are given in the text.

Ion	Charge (HF)	Charge (NO-SDCI)
Mn	2.37	2.23
O (xy-plane)	−1.75	−1.72
O ($\pm z$)	−1.68	−1.67

electron–phonon interactions are JT active. Our HF and CI calculations do not show any significant t_{2g} $^4T_{2g}$ instability; therefore, in what follows we concentrate on the e_g-mode coupling. Jahn–Teller energies and frequencies have been obtained by fitting the corresponding potential energy curves (PEC) with polynomials defined up to sixth order in the JT-mode displacements. Whereas in the case of HF-PEC we obtained good quality fits (corresponding to mean deviations <0.01 eV) even in the harmonic approximation (i.e. employing parabolas), it was necessary to consider sixth-order terms for CI-PEC in order to maintain the quality of our fits. This result suggests that correlation effects increase the anharmonic potential terms. Table 5 compiles our calculations of e_g-mode couplings. All of the results are based on the best fits employing sixth-order polynomials. The frequencies have been obtained from Taylor expansions to second order around the respective curve minima. Inspection of table 5 shows that the introduction of correlation lowers E_{JT} and increases the vibration frequencies. An analogous influence on frequencies can also be observed in the case of the breathing-mode a_{1g} $^4A_{2g}$ electron–phonon couplings (HF: 830

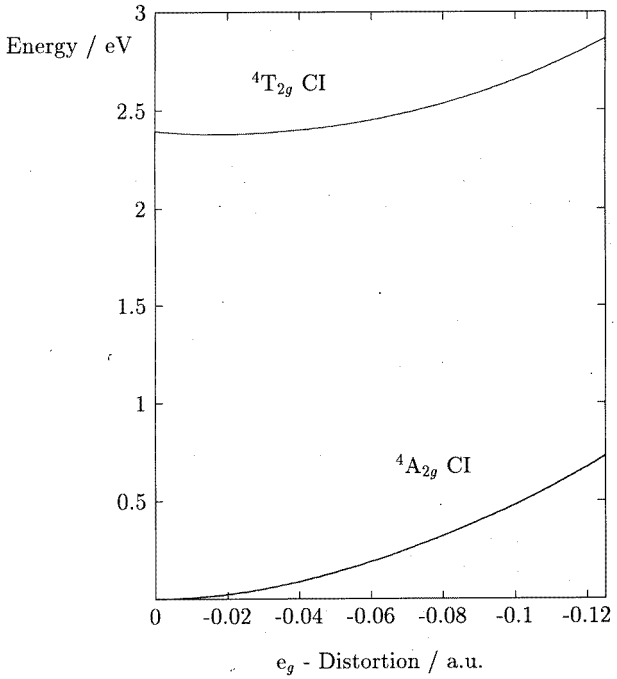

Figure 4. A configuration diagram displaying the energy dependence of the $^4A_{2g}$ and $^4T_{2g}$ states upon e_g-type ligand distortions δ_{e_g}.

cm^{-1}; CI: 980 cm^{-1}). Table 6 displays calculated ion charges which have been obtained from a Mulliken population analysis (MPA) for the excited $^4T_{2g}$ state. These results are based on HF and NO-SDCI charge densities which have been calculated employing the a_{1g} relaxed $^4T_{2g}$(CI) lattice. The occupied Mn^{4+} e_g orbital corresponds to $d_{x^2-y^2}$. We emphasize the relative merit of MPA charges according to which only the differences between the HF and CI analyses are physically significant, and not the calculated ion charges. It can be seen that CI increases the charge transfer onto the central manganese cation which results in an enhanced bonding stiffness and, thus, leads to the prediction of higher JT frequencies; at the same time, correlation reduces the charge differences between the xy-planar oxygen ions and the ones along $\pm z$ which is in line with a reduction of the JT distortion δ_{e_g}. Figure 3 shows our calculated $^4T_{2g}$ total HF and CI energies as a function of an e_g JT distortion. Figure 4 displays a configuration diagram related to the e_g mode.

Finally, our simulations of JT distortions suggest a pronounced dynamical behaviour, since the JT energies are small in comparison with the frequencies.

3.3. Stability and charge-transfer transitions

In this section we comment on the relative stability of Mn^{4+}_{Ti} defect centres in $BaTiO_3$. The major questions that we are going to discuss concern the possible interpretation of orbital energies derived from cluster calculations. We will review the assertion that only differences in total cluster energies (ΔSCF) are physically relevant. Since the pioneering investigations on transition-metal complexes [33–36] it has become clear that orbital energies may be highly misleading. In spite of this knowledge there are even today publications which

put some emphasis on cluster orbital energies (see, for example, [37–40]) or, at least, the ascribed meanings of the orbital energies presented remain diffuse [41].

Returning to the stability of Mn^{4+}, we, finally, employ the ΔSCF procedure to investigate the energetics of charge-transfer reactions, which involve an electron transfer from the oxygen ligand sphere onto the manganese cation.

By inspection of the orbital energies of the central $(MnO_6)^{8-}$ cluster we observed the singly occupied $d(t_{2g})$ levels of the manganese below all doubly occupied oxygen 2p levels corresponding to an energy separation of $\sim$10 eV between the d orbitals and the top of the 'valence band' states. At first glance this situation seems to reflect a highly excited electronic state and one might guess that tetravalent manganese is extremely unstable against charge transfer. However, two important facts should be borne in mind. First, the cluster eigenvalues do not correspond to crystalline eigenstates! Thus, principally the cluster eigenvalues do not provide any information on the positions of defect levels within the band gap. Generally, the justification of any embedded-cluster calculation starts by considering the total crystalline one-electron Hamiltonian (within Hartree–Fock or Kohn–Sham theory), which is diagonal in the delocalized Bloch orbital representation. In the case of insulators in which we are interested there are always unitary transformations between the occupied Bloch orbitals and an equal number of localized orbitals [42]. It is therefore possible to obtain an equivalent representation of the one-electron Hamiltonian employing the (occupied) localized orbitals. Accordingly, the total crystalline electron density is given by

$$\rho(\boldsymbol{r}) = \sum_{n,\boldsymbol{R}}^{occ} |\omega_n(\boldsymbol{r} - \boldsymbol{R})|^2 \tag{7}$$

where the sum runs over the occupied orbitals $\omega_n(\boldsymbol{r} - \boldsymbol{R})$ belonging to the band index n and centred around $\boldsymbol{R}$. Equation (7) provides the basis for separating the solid into a cluster which is embedded in an outer host crystal. The additional introduction of a defect does not cause any problems as long as the defect states are sufficiently localized. Next it is important to realize that the one-electron problem formulated with localized orbitals is no longer diagonal. However, the procedure of Kunz and Klein [43] demonstrates that the off-diagonal Lagrange multipliers may be interpreted as short-range embedding potentials which define the proper cluster boundary conditions. The remaining diagonal Lagrange multipliers represent the eigenvalues of the embedded cluster. Up to this point our brief discussion shows that eigenvalues of (small) clusters are not simply related to crystalline eigenvalues†. The second remark concerns the physical significance of orbital energies of small quantum systems such as atoms or molecular clusters. Within HF theory it is Koopmans' theorem which identifies the orbital energies with negative ionization energies. Orbital energy differences are then approximate excitation energies. However, there is a precondition for this theorem to work practically, i.e. excitation-induced orbital relaxation effects must be negligibly small. Whereas this condition is fulfilled for delocalized eigenstates of large systems like crystals, it is not guaranteed for small clusters of atoms. As an example we consider the present $(MnO_6)^{8-}$ cluster: first, we self-consistently calculated the $^4A_{2g}$ electronic state of this cluster. Then, without allowing any further orbital relaxations, we calculated the two ionized states with one electron removed either from the top of the oxygen

† By extending the cluster size to infinity one would certainly observe that the cluster orbitals (and energies) converge to their bulk limits. This relation provides information on how fast the cluster orbitals approach the delocalized crystalline eigenstates. Typically one must consider large clusters in order to obtain the properties of delocalized bulk orbitals. This observation, however, does not invalidate (small) embedded-cluster calculations, because their justification derives from the use of localized crystalline orbitals based on equation (7).

2p levels or from the $d(t_{2g})$ manganese orbitals. The total energy differences with respect to the $^4A_{2g}$ state provide the corresponding ionization energies. We therefore forced the precondition of Koopmans' theorem to be operative. The difference between the ionization energies obtained in this way ($\sim$10 eV) equals the difference of orbital energies quoted above. Next we repeated the calculation of the ionization energies but taking into account orbital relaxations. As a result of orbital relaxations (which mainly affect the ionization from the localized d orbitals corresponding to an energy gain of $\sim$7.1 eV) the difference of ionization energies for the two processes reduces to about 3.9 eV. Thus, the ΔSCF method shifts the $d(t_{2g})$-related states of manganese much closer to the oxygen 2p states. Related discussions of the breakdown of Koopmans' theorem in transition-metal complexes are reported in [44–46].

We emphasize that ΔSCF energies may be considered as simplified cases of total crystal energy differences calculated on the basis of equation (5), if the individual total energies differ only with respect to the cluster state function Ψ. In this fashion, differences between SCF energies are the physically relevant quantities which are consistent with the embedded-cluster approach, and not orbital energy differences. The situation differs slightly in the case of embedded-cluster calculations based on the X_α exchange approximation [47] or, more generally, on the density functional theory (DFT). Again, *a priori* the cluster orbital energies are not related to crystalline one-electron energies. But differently to the HF case, there is from the beginning no formal basis for Koopmans' theorem relating the one-electron energies to (unrelaxed) ionization energies. Instead, the theorem of Slater [47] (generalized for DFT by Janak [48]) holds:

$$\epsilon_i = \frac{\partial E[\rho]}{\partial n_i}. \tag{8}$$

For large numbers of electrons this theorem provides a relation between orbital energies ϵ_i and corresponding occupation numbers n_i according to the Fermi–Dirac statistics. It is, thus, plain that the different meanings of HF and X_α one-electron energies may result in a substantially different level ordering. As an example we compare our HF orbital energies with corresponding ones obtained from earlier X_α cluster calculations on $(MnO_6)^{8-}$ [54]. Whereas within the HF model the $d(t_{2g})$ manganese orbital energies are well separated from the oxygen 2p levels, the same d orbital energies are close to the top of the oxygen 2p states in the case of the X_α cluster calculations. Following Slater [47] the differences between the orbital energies can be traced back to the differences between the respective exchange potentials:

$$\epsilon_i^{X_\alpha} - \epsilon_i^{HF} = V_{X_\alpha}(\boldsymbol{r}) - V_{XHF,i}(\boldsymbol{r}). \tag{9}$$

The inspection of Slater–Condon exchange parameters of transition-metal atoms suggests that the 3p–3d exchange interaction is particularly responsible for the expected differences between the exchange potentials.

Both the HF and the X_α one-electron energies are qualitatively related to an ionization, i.e. the first ones on the basis of Koopmans' theorem and the latter ones as a consequence of the Fermi–Dirac statistics (the highest occupied orbitals should be most easily ionizable). It may be assumed that X_α and HF orbital energies represent lower and upper bounds to the true ionization energy based on ΔSCF which, however, can be substantially different from the orbital energies, if the difference on the left-hand side of equation (9) is large. Then we have to expect considerable orbital relaxation effects. Only in situations of delocalized orbitals can we expect the difference between the X_α and HF exchange potentials to be sufficiently small. The corresponding agreement of orbital energies then leads to a physical

interpretation of the one-electron energies, since both Koopmans' theorem and the Fermi–Dirac condition are approximately fulfilled. This situation corresponds to crystalline one-electron eigenstates close to the Fermi energy and agrees with general perceptions of DFT.

In summary, there are two main reasons for which physical interpretations of embedded-cluster calculations should not be based on cluster orbital energies. First, cluster eigenvalues correspond to localized crystal orbitals and are thus not directly related to the crystalline eigenstates which provide the information on the defect levels in the band gap. Second, orbital relaxation effects generally prevent a useful interpretation being made of cluster eigenvalues as ionization energies.

Table 7. The energy separation (eV) between CT states and the Mn^{4+} ground state $^4A_{2g}$, $\Delta E = E(\mathrm{CT}) - E(^4A_{2g})$. Columns a and b refer to the high-spin configuration $t_{2g}^3 e_g$ and to the low-spin configuration t_{2g}^4 of Mn^{3+}, respectively. The energies have been obtained from UHF calculations, whereas the numbers in brackets refer to ROHF results. In the case of relaxed lattices each electronic state has been calculated within its own equilibrium lattice geometry.

Lattice	a	b
Perfect	1.40 (1.13)	3.21
Relaxed	0.77 (0.5)	2.66

Finally, in order to establish the relative stability of the Mn_{Ti}^{4+} centres it is necessary to investigate charge-transfer (CT) reactions involving an electron transfer from the oxygen ligands onto the manganese cation. These CT calculations have been performed employing perfect-lattice spacings as well as relaxed lattice structures. For the latter type of calculation we adopted a further approximative relaxation procedure in order to account for symmetry-reducing lattice distortions accompanying the CT states. This method goes beyond the treatment of JT distortions as outlined in section 3.2, since it allows the symmetry-reducing lattice displacements to occur for all cluster ions and not only for the ligand anions. Such a generalization seems to be necessary, because the modifications of the oxygen electron structure due to CT are obviously more pronounced than in the case of the $^4T_{2g}$ CF state. The outer crystal lattice represented by 736 point ions with integral charges has been held fixed corresponding to the relaxed crystal structure which is in equilibrium with the Mn^{4+} $^4A_{2g}$ HF ground state. The cluster relaxation has been performed using the geometry optimization facilities of the HONDO 7.0 *ab initio* code. For this task the program has been modified in order to include short-range Buckingham potentials between cluster ions and embedding point charges. Table 7 lists the corresponding total energy differences (see equation (5)) between the CT states and the Mn^{4+} $^4A_{2g}$ state. The CT states invoke the formation of Mn^{3+} for which we assumed two possible configurations, i.e. the high-spin configuration $t_{2g}^3 e_g$ (^5E_g) and the low-spin configuration t_{2g}^4 ($^3T_{1g}$). The columns a and b in table 7 refer to these situations, respectively. The difference of these energies measures the energy separation between the two Mn^{3+} crystal-field states. The Mn^{3+} high-spin configuration is more favourable by 1.8–1.9 eV than the low-spin configuration. In the case of the high-spin configuration of Mn^{3+} the created hole localizes on the two oxygen anions along $\pm z$, because the occupied Mn^{3+} e_g orbital corresponds to $3z^2 - r^2$. In this case the electronic structure of the acceptor-type cation (Mn^{3+}) determines the localization properties of the associated hole. More generally, it would be important to investigate the hole localization as a function of size, charge state and electronic structure of the trapping acceptor defect. For example, in suitable cases the trapping of two holes may be more favourable than the association of only one hole which can initiate the formation of hole-type bipolarons.

This has recently been shown for Mg^{2+}_{Ti} acceptor cations [49]. Photo-ESR (electron spin-resonance) experiments provided evidence that trapped holes play an important role in the photorefractive mechanisms in $BaTiO_3$ [50].

Table 7 shows that Mn^{4+} is stable against CT, since the $^4A_{2g}$ ground state of Mn^{4+} represents the most favourable electronic state irrespective of the inclusion of lattice relaxation. However, lattice relaxations lead to a reduction of the respective energy separations. This is reasonable, because Mn^{4+} is almost identical to the substituted Ti^{4+}; the CT state, on the other hand, defines a comparatively larger perturbation of the local crystal structure which needs stronger lattice relaxations for its compensation or screening. The additional influence of electronic correlations has been investigated on the basis of Møller–Plesset perturbation calculations to second order (MP2) and DFT. We used MP2 instead of costly CI expansions, because the CADPAC code employed allows one to perform 'direct' MP2 calculations, which significantly reduces the necessary computer storage capacities. The direct feature becomes particularly helpful as the the basis set considered becomes more extended. Qualitatively, the effect of correlations may be understood on the basis of increased covalency between the oxygen anions and the manganese cation. In comparison to the HF case, electrons on the anions become more stabilized, but destabilized on the cation. As a consequence the CT states are shifted to higher energies. Preliminary MP2 calculations, which employ the previous basis set (see section 2) as well as perfect-lattice spacings, indicated a corresponding energy shift of about 0.6 eV (see also below).

Finally, we calculated the energy separations between the Mn^{4+} $^4A_{2g}$ state and the lowest CT state involving for both states consistently either the $^4A_{2g}$ relaxed lattice or the CT relaxed lattice. In the first situation the energy separation corresponds to optical absorption and in the second case it corresponds to optical emission. Within the UHF approximation we obtained 1.1 eV as the onset value for the CT optical absorption, and 0.4 eV correspondingly for the CT optical emission. First, we observe that CT transitions are characterized by large Stokes shifts. As expected this is different from the crystal-field transitions discussed in section 3.2. Second, however, the calculated onset energy of the CT optical absorption is somewhat smaller than reported experimental energies (>3.2 eV) referring to $SrTiO_3$:Mn^{4+}_{Ti} [31]. In particular, the CT absorption energy is significantly smaller than the $^4T_{2g}-{}^4A_{2g}$ transition energy, which contradicts the experiments. We emphasize that our predicted energy corresponds to the HF approximation and we suggest that the inclusion of electron correlations is necessary and sufficient for calculating accurate CT transition energies.

MP2 calculations based on the previous basis set (see section 2) and employing the $^4A_{2g}$ equilibrated crystal lattice yield 2.0 eV for the CT optical absorption. This value represents a lower bound to the true CT energy, because unlike the crystal-field-splitting energies the CT transition energies have been found to be highly dependent on the quality of the basis set used. The reason for this different behaviour is based on the pronounced charge redistributions accompanying CT. The accurate simulation of CT, therefore, needs a very flexible basis set. For example, using a full-orbital, split-valence basis set for the manganese cation, retaining the previous description of the oxygen anions (see section 2) and, finally, augmenting this basis set with additional oxygen and manganese d-type functions increases the UHF and MP2 CT absorption energies to 1.7 eV and 3.3 eV, respectively. It is noticed that even with this sophisticated basis set the UHF CT absorption energy is significantly smaller than the $^4T_{2g}-{}^4A_{2g}$ CF transition energy which contradicts all relevant experience. But, noticeably, in this case MP2 predicts a reasonable CT absorption energy which is significantly greater than the $^4T_{2g}-{}^4A_{2g}$ CF splitting and which satisfactorily agrees with reported experimental data for $SrTiO_3$:Mn^{4+}_{Ti} [31].

In order to extend the description of correlation contributions and to keep the required computer capacities manageable at the same time, further simulations have been done on the basis of density functional theory (DFT). According to Perdew and Levy [51] every extremum density of the ground-state energy functional yields the exact energy of a stationary state. Whereas the absolute minimum corresponds to the ground state, the other extrema represent a subset of the excited states. Exact densities which do not extremize the ground-state functional, however, provide lower bounds to the corresponding excited-state energies, i.e. $E[\rho_i] < E_i$ where i refers to any such excited state. Further, the set of extremum densities of the ground-state functional generally forms a subset of all stationary densities which may be obtained by applying the usual Kohn–Sham approach. However, if the Kohn–Sham densities provide reasonable approximations to exact densities one may use the above-stated inequality in order to estimate the required energy separations.

Keeping this information in mind we calculated the $^4A_{2g}$, $^4T_{2g}$ and the CT electronic state energies employing the $^4A_{2g}$-state equilibrated lattice geometry which has been derived earlier within HF theory. For these DFT calculations we used the CADPAC code [19] which employs the Kohn–Sham procedure. The computational implementation involves Gaussian-type basis functions and a numerical quadrature of all integrals which are related to the effective one-electron exchange–correlation potential. The present calculations employed the same sophisticated basis set as the MP2 calculations discussed above. In order to approximate the unknown exact exchange–correlation functional an advanced functional has been used which combines the exchange functional due to Becke [52] and the correlation functional derived by Lee, Yang and Parr [53]. It is emphasized that this exchange–correlation functional significantly improves on the commonly employed local density approximation. The results of the present DFT simulations are encouraging: whereas the $^4T_{2g}$ state is 2.1 eV above the $^4A_{2g}$ ground state, the CT absorption energy becomes 3.4 eV. These energy separations, which are expected to give lower bounds to the true excited-state separations from the ground state, are in good agreement with the corresponding values obtained from the SDCI + Q and MP2 calculations discussed above. Most importantly we notice that the CT absorption energy is at least 1.2 eV greater than the respective CF transition energy. Experimentally, for $SrTiO_3$:Mn^{4+} a corresponding energy separation of $\sim$1 eV has been observed [31]. The remarkable quality of the present DFT results may at least partly be traced back to significant electron density differences between the required states. However, it is recalled in this context that there are also situations where DFT fails to give reliable excited-state estimates. Most prominent is the inability of DFT to reproduce the atomic multiplet structure [51].

In conclusion we observe that electron correlation contributions are necessary and sufficient in order to reliably simulate CT transitions related to transition-metal impurities in $BaTiO_3$. The suggested embedded-cluster approach gives useful CT transition energies provided that the set of basis functions employed is sufficiently flexible. In this context we also briefly comment on the occurrence of symmetry-broken CT states within HF theory which simulate a complete hole localization at exactly one of the oxygen ligand anions. These localized CT states, though representing in many cases the most favourable HF states, do not indicate the instability of particular impurity charge states in $BaTiO_3$, but refer to a general instability due to HF theory which is a manifestation of the so-called symmetry dilemma. On the other hand, the symmetrized CT states discussed so far reflect the stability properties of impurity cations in $BaTiO_3$ at least qualitatively. In fact, after inclusion of sufficient electron correlations the symmetrized CT solutions represent the most favourable CT states for all transition-metal cations investigated. On the basis of this observation we have discarded the localized CT states from the present considerations in order to avoid

these additional HF-specific problems. A detailed discussion will, however, be presented in a forthcoming publication.

Moretti and Michel-Calendini [54] reported a calculated CT transition energy of ∼2.8 eV. These cluster calculations were based on the X_α exchange approximation and on perfect-lattice spacings. Further, these investigations neglected any correlation contributions. We do not know the precise reasons for which our best UHF-based energy threshold is about 1 eV smaller, but it could be that the local X_α exchange potential underestimates the gain in exchange energy between t_{2g}- and e_g-type electrons which occurs upon forming the Mn^{3+}. Moreover, certain shortcomings could also be due to the muffin-tin potential approximation employed.

4. Conclusion

Using an embedded-cluster description we are able to reliably calculate the local electronic properties of transition-metal cations incorporated into the perovskite-structured oxide $BaTiO_3$. The defect cluster consisting of 21 atoms is characterized on the basis of a LCAO-SCF-MO approach. Our calculations consistently employed Hartree–Fock theory and configuration interactions. The results are exemplified for Mn^{4+} transition-metal cations. The embedding lattice is represented by a shell-model description. The explicit account of lattice relaxations facilitates the calculation of absorption and emission energies related to crystal-field and charge-transfer transitions. In particular, the calculation of charge-transfer transitions necessitates the inclusion of electron correlations.

Acknowledgments

The financial support of this work by the Deutsche Forschungsgemeinschaft (SFB 225) is gratefully acknowledged. We are indebted to Professor O F Schirmer for encouraging us to make these investigations. Further, we gratefully acknowledge the many helpful discussions with Dr Amanda Woods and Dr Robert Sinkovits.

References

[1] Günter P and Huignard J-P (ed) 1988 *Photorefractive Materials and their Application I and II (Springer Topics in Applied Physics 61, 62)* (Berlin: Springer)
[2] Fainman Y, Ma J and Lee S H 1993 *Mater. Sci. Rep.* **9** 53
[3] Mooradian A, Jaegar T and Stokseth P 1976 *Tunable Lasers and Applications* (Berlin: Springer)
[4] Vail J M 1990 *J. Phys. Chem. Solids* **51** 589
[5] Zuo Jun, Pandey R and Kunz A B 1991 *Phys. Rev.* B **44** 7187
[6] Woods A M, Sinkovits R S, Charpie J C, Huang W L, Bartram R H and Rossi A R 1993 *J. Phys. Chem. Solids* **54** 543
[7] Woods A M, Sinkovits R S and Bartram R H, 1994 *J. Phys. Chem. Solids* **55** 91
[8] Gryk T J and Bartram R H 1995 *J. Phys. Chem. Solids* **56** 863
[9] Donnerberg H and Bartram R H 1994 *J. Lumin.* **60 & 61** 162
[10] Müller K A, Berlinger W and Blazey K W 1987 *Solid State Commun.* **61** 21
[11] Müller K A 1986 *Helv. Phys. Acta* **59** 874
[12] Hay W R and Wadt P J 1985 *J. Chem. Phys.* **82** 270
[13] Dunning T H and Hay P J 1977 *Methods of Electronic Structure Theory* ed H F Schaefer III (New York: Plenum) ch 1, pp 1–27
[14] Rawlings D C and Davidson E R 1983 *Chem. Phys. Lett.* **98** 424
[15] Davidson E R and Silver D W 1977 *Chem. Phys. Lett.* **52** 403
[16] Bender C F and Davidson E R 1966 *J. Phys. Chem.* **70** 2675

[17] Davidson E R 1991 *QCPE 23, Program No 580*
[18] Dupuis M, Watts J D, Villar H O and Hurst G J B 1991 *QCPE 23, Program No 544*
[19] Amos R D *et al* 1994 *Cambridge Analytic Derivatives Package (CADPAC)* version 5.2 (Cambridge)
[20] Dick B G and Overhauser A W 1958 *Phys. Rev.* **112** 90
[21] Mott N F and Littleton M J 1938 *Trans. Faraday Soc.* **34** 485
[22] Leslie M 1983 *Solid State Ion.* **8** 243
[23] Catlow C R A and Mackrodt W C (ed) 1982 *Computer Simulation of Solids (Springer Lecture Notes in Physics 166)* (Berlin: Springer)
[24] Lewis G V and Catlow C R A 1986 *J. Phys. Chem. Solids* **47** 89
[25] McWeeny R 1959 *Proc. R. Soc.* A **253** 242; 1989 *Methods of Molecular Quantum Mechanics* (London: Academic)
[26] Huzinaga S and Cantu A A 1971 *J. Chem. Phys.* **55** 5543
[27] Sinkovits R S and Bartram R H 1991 Modification of HADES III, unpublished
Donnerberg H 1992 Modification of CASCADE, unpublished
[28] Shannon R D and Prewitt C T 1969 *Acta Crystallogr.* B **25** 925
[29] Sangster M J L 1981 *J. Phys. C: Solid State Phys.* **14** 2889
[30] Groh D J, Pandey R and Recio J M 1994 *Phys. Rev.* B **50** 14860
[31] Blasse G, De Korte P H M and Mackor A 1981 *J. Inorg. Nucl. Chem.* **43** 1499
[32] Stokowski S E and Schawlow A L 1969 *Phys. Rev.* **178** 2, 457
[33] Ellis D E, Freeman A J and Ros P 1968 *Phys. Rev.* **176** 688
[34] Kleinman B and Karplus M 1971 *Phys. Rev.* B **3** 24
[35] Soules T F, Richardson J W and Vaught D M 1971 *Phys. Rev.* B **3** 2186
[36] Richardson J W, Soules T F, Vaught D M and Powell R P 1971 *Phys. Rev.* B **4** 1721
[37] Moretti P and Michel-Calendini F M 1988 *J. Opt. Soc. Am.* B **5** 1697
[38] Michel-Calendini F M and Bellafrouh K 1992 *Ferroelectrics* **125** 271
[39] Qiu Yuanwu 1993 *J. Phys.: Condens. Matter* **5** 2041
[40] Bermejo M, Recio J M, Luaña V and Pueyo L 1991 *Radiat. Eff. Defects Solids* **119–121** 441
[41] Meng J, Vail J M, Stoneham A M and Jena P 1990 *Phys. Rev.* B **42** 1156
[42] Bar'yudin L É 1991 *Sov. Phys.–Solid State* **33** 1820
[43] Kunz A B and Klein D L 1978 *Phys. Rev.* B **17** 4614
[44] Guest M F and Saunders V R 1975 *Mol. Phys.* **29** 873
[45] Hillier T H 1979 *Pure Appl. Chem.* **51** 2183
[46] Veillard A and Demuynk J 1977 *Modern Theoretical Chemistry* vol 4, ed H F Schaeffer (New York: Plenum)
[47] Slater J C 1974 *The Self-consistent Field for Molecules and Solids* vol 4 (New York: McGraw-Hill)
[48] Janak J F 1978 *Phys. Rev.* B **18** 7165
[49] Donnerberg H and Birkholz A 1995 *J. Phys.: Condens. Matter* **7** 327
[50] Possenriede E, Jacobs P, Kröse H and Schirmer O F 1992 *Appl. Phys.* A **55** 73
[51] Perdew J P and Levy M 1985 *Phys. Rev.* B **31** 6264
[52] Becke A D 1988 *Phys. Rev.* A **38** 3098
[53] Lee C, Yang W and Parr R G 1988 *Phys. Rev.* B **37** 785
[54] Moretti P and Michel-Calendini F M 1986 *Phys. Rev.* B **34** 8538